Journal of Applied Physics

RESEARCH ARTICLE | MARCH 22 2024

Impact of strain on the SOT-driven dynamics of thin film Mn_3Sn

Ankit Shukla ; Siyuan Qian ; Shaloo Rakheja

J. Appl. Phys. 135, 123903 (2024)
https://doi.org/10.1063/5.0179669

AIP Publishing

Journal of Applied Physics ARTICLE pubs.aip.org/aip/jap

Impact of strain on the SOT-driven dynamics of thin film Mn_3Sn

Cite as: J. Appl. Phys. **135**, 123903 (2024); doi: 10.1063/5.0179669
Submitted: 4 October 2023 · Accepted: 6 March 2024 ·
Published Online: 22 March 2024

Ankit Shukla,[a] Siyuan Qian,[b] and Shaloo Rakheja[c]

AFFILIATIONS

Holonyak Micro and Nanotechnology Laboratory, University of Illinois at Urbana-Champaign, Urbana, Illinois 61801, USA

[a]**Author to whom correspondence should be addressed:** ankits4@illinois.edu
[b]**Electronic mail:** siyuanq3@illinois.edu
[c]**Electronic mail:** rakheja@illinois.edu

ABSTRACT

Mn_3Sn, a metallic antiferromagnet with an anti-chiral 120° spin structure, generates intriguing magneto-transport signatures such as a large anomalous Hall effect, spin-polarized current with novel symmetries, anomalous Nernst effect, and magneto-optic Kerr effect. When grown epitaxially as MgO(110)[001]|| $Mn_3Sn(0\bar{1}\bar{1}0)[0001]$, Mn_3Sn experiences a uniaxial tensile strain, which changes the bulk sixfold anisotropy to a twofold perpendicular magnetic anisotropy (PMA). Here, we investigate the field-assisted spin–orbit-torque (SOT)-driven dynamics in single-domain Mn_3Sn with PMA. We find that for non-zero external magnetic fields, the magnetic octupole moment of Mn_3Sn can be switched between the two stable states if the input current is between two field-dependent critical currents. Below the lower critical current, the magnetic octupole moment exhibits a stationary state in the vicinity of the initial stable state. On the other hand, above the higher critical current, the magnetic octupole moment shows oscillatory dynamics which could, in principle, be tuned from the 100s of megahertz to the terahertz range. We obtain approximate analytic expressions of the two critical currents that agree very well with the numerical simulations for experimentally relevant magnetic fields. We also obtain a unified functional form of the switching time vs the input current for different magnetic fields. Finally, we show that for lower values of Gilbert damping ($\alpha \lesssim 2 \times 10^{-3}$), the critical currents and the final steady states depend significantly on α. The numerical and analytic results presented in our work can be used by both theorists and experimentalists to understand the SOT-driven order dynamics in PMA Mn_3Sn and design future experiments and devices.

I. INTRODUCTION

Antiferromagnets (AFMs) are a class of magnetic materials that produce negligible stray fields, are robust to external magnetic field perturbations, and exhibit resonant frequency in the terahertz (THz) regime. These distinctive properties are a consequence of strong exchange interactions between the uniquely arranged spins of the neighboring atoms and a negligible net macroscopic magnetization.[1–4] AFMs are, therefore, considered promising candidates for building next generation magnonic devices, high-density memory devices, and ultrafast signal generators.[5] Among the various possible AFMs, noncollinear but coplanar metallic AFMs of the form Mn_3X, with a triangular spin structure, have recently been explored extensively owing to their intriguing magneto-transport characteristics, such as a large spin Hall effect (SHE),[6] anomalous Nernst effect (ANE), anomalous Hall effect (AHE),[7–10] magneto-optical Kerr effect (MOKE),[11] ferromagnet-like spin-polarized currents,[12,13] and a finite tunneling magnetoresistance (TMR).[14,15] These noncollinear AFMs are chiral in nature and could be further classified as positive (X = Ir, Pt, Rh) or negative (X = Sn, Ge, Ga) chirality materials based on the type of spin interaction.[16]

Here, we focus on thin-film Mn_3Sn, owing to its various technologically relevant properties. Bulk Mn_3Sn, which is a sixfold spin-degenerate chiral antiferromagnet with a small net magnetization, has a high Néel temperature of approximately 420–430 K.[11,17,18] Recent experiments have demonstrated that the magnetic order parameter in Mn_3Sn, referred to as the magnetic octupole moment, can be switched between the six stable states using spin–orbit torque (SOT) in a bilayer setup of AFM and heavy metal (HM).[19–23] The critical charge current density

required to switch the magnetic octupole moment was found to be of the order of 10^6-10^7 A/cm^2, which is smaller than or comparable to that required to switch the magnetization in most ferromagnets ($\sim 10^7-10^8$ A/cm^2).[24] Some experiments have also alluded to current-driven oscillations of the octupole moment, with frequencies in the range of 100s of MHz to a few GHz, in the bilayer setup.[20,25] In all of these experiments, the changes in the octupole moment were detected via the AHE since Mn_3Sn exhibits large anomalous Hall conductivity, ranging between 30 and 40 Ω^{-1} cm^{-1} at 300 K, owing to the broken time-reversal symmetry (TRS).[7,26,27] The magnitude and sign of the AHE signal can be further modulated by the application of small in-plane tensile or compressive uniaxial strain of the order of 0.1%, as revealed recently.[28] Such uniaxial strains alter the crystal symmetry, followed by the spin degeneracy and, hence, the Hall conductivity.[28,29]

Thin films of Mn_3Sn, when grown epitaxially on MgO(110)[001] substrate, also experience in-plane tensile strain, arising from the lattice mismatch between Mn_3Sn and MgO. Consequently, the sixfold spin-degenerate system reduces to a twofold spin-degenerate system, with a comparatively larger net magnetization, leading to perpendicular magnetic anisotropy (PMA) in such films.[30,31] The AHE measurements further revealed that the magnetic octupole moment of the PMA Mn_3Sn films, used in a bilayer setup, can be deterministically switched in the presence of a symmetry-breaking magnetic field, which is parallel to the current direction.[30,31] Recently, all antiferromagnetic tunnel junctions comprising Mn_3Sn/MgO/Mn_3Sn, utilizing PMA Mn_3Sn, were found to display non-zero TMR of about 2% at room temperature—owing to the TRS breaking and the momentum-dependent spin splitting of electronic band structure.[15,32] These promising developments make thin-film PMA Mn_3Sn a strong candidate for future high-density memory and ultrafast nano-oscillator devices.

For a better understanding of the current-driven dynamics, on the theoretical front, Higo *et al.* presented a brief numerical investigation of the different possible steady states in PMA Mn_3Sn, as a function of the applied current and magnetic field.[30] Their study, however, is limited in its scope as it does not provide an insight into the dependence of the different dynamical regimes on the intrinsic energy scale of Mn_3Sn or its material parameters. Analytic expressions of threshold currents, switching times, and oscillation frequency as functions of material parameters and input stimuli are also lacking. Another recent work, focusing on Mn_3Sn with uniaxial strain, numerically investigated only the field-free oscillation and pulsed-SOT switching dynamics.[29] In their very recent work, Yoon and Zhang *et al.* developed analytic models of the first- and second-harmonic Hall resistances and successfully validated them against experimental observation.[31] Their analysis, however, was limited to the quasi-static regime. Previous theoretical works have also explored current-driven switching and oscillation dynamics in AFMs with twofold spin degeneracy.[33–35] However, those materials were not representative of Mn_3Sn with uniaxial strain since the net magnetization was considered zero. In this work, therefore, we address the existing limitations and investigate, both numerically and analytically, the magnetic field-assisted SOT-driven deterministic switching and oscillation dynamics in monodomain Mn_3Sn, with two stable states.

For the numerical investigation of the static and dynamic properties of single-domain Mn_3Sn with in-plane uniaxial strain, an energy interaction model is presented in Sec. II of this work. To elucidate the properties of the ground states as well as their dependence on the material parameters, a simpler analytic model of the energy interaction is perturbatively obtained in Sec. II A and shown to agree well with the numerical results. Next, the field-assisted SOT-driven dynamics of the magnetic order in PMA Mn_3Sn is analyzed in Sec. III. Analytic models, pertinent to the current-driven dynamics such as threshold currents, stationary states, switching time, and oscillation frequency, are presented in detail. Previously, we had utilized this framework to analyze field-free SOT-driven dynamics in monodomain Mn_3Sn with six states.[36] In our present work, however, we build models that elucidate the impact of strain as well as magnetic field on the dynamics. The impact of the Gilbert damping constant on the dynamics is investigated and the salient features are discussed in Sec. IV. The field-assisted SOT-driven dynamics in Mn_3Sn with no strain[37] and compressive strain is discussed in the supplementary material, along with a brief discussion on the AHE and the TMR detection schemes.

II. FREE ENERGY MODEL AND GROUND STATES

Below its Néel temperature, Mn_3Sn crystallizes into a hexagonal Kagome $D0_{19}$ lattice and can only be stabilized in slight excess of Mn atoms. The Mn atoms are located at the corners of the hexagons, whereas the Sn atoms are located at their respective centers. Such lattices are stacked along the c axis ([0001] direction) in an ABAB arrangement. A simple representation of the crystal structure is presented in Fig. 1. In each Kagome plane, the magnetic moments on the Mn atoms form a geometrically frustrated noncollinear triangular spin structure [Fig. 1(a)], with spins on the nearest neighbors aligned at an angle of approximately 120° with respect to each other.[17] These spins are canted slightly toward the in-plane easy axes, resulting in a small net magnetization, which is sixfold degenerate in the Kagome plane.[26] Under the application of a small in-plane uniaxial strain, the system becomes twofold degenerate, and its net magnetization is also altered.[28,30,31]

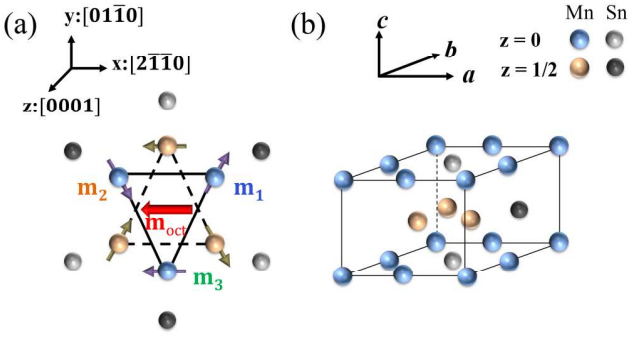

FIG. 1. (a) Atomic and one of the six possible spin arrangements in the basal plane of bulk Mn_3Sn. (b) Unit cell of Mn_3Sn.

To investigate the static and the current-driven dynamic behavior of a single-domain particle of uniaxially strained-Mn_3Sn, comprising three interpenetrating sublattices, the free energy density is defined as[28,30]

$$F(\mathbf{m}_1, \mathbf{m}_2, \mathbf{m}_3) = J_E((1+\delta_E)\mathbf{m}_1 \cdot \mathbf{m}_2 + \mathbf{m}_2 \cdot \mathbf{m}_3 + \mathbf{m}_3 \cdot \mathbf{m}_1) + D_M \mathbf{z} \cdot (\mathbf{m}_1 \times \mathbf{m}_2 + \mathbf{m}_2 \times \mathbf{m}_3 + \mathbf{m}_3 \times \mathbf{m}_1) - \sum_{i=1}^{3} \left(K_e(\mathbf{m}_i \cdot \mathbf{u}_{e,i})^2 + M_s \mathbf{H}_a \cdot \mathbf{m}_i\right), \quad (1)$$

where $\mathbf{m}_1$, $\mathbf{m}_2$, and $\mathbf{m}_3$ are the magnetization vectors corresponding to the three sublattices, while $J_E(>0)$, $D_M(>0)$, and $K_e(>0)$ are the symmetric exchange interaction constant, asymmetric Dzyaloshinskii–Moriya interaction (DMI) constant, and single-ion uniaxial magnetocrystalline anisotropy constant, respectively. Each magnetization vector has a constant saturation magnetization, M_s. Here, it is assumed that the uniaxial strain acts between $\mathbf{m}_1$ and $\mathbf{m}_2$. The effect of this uniaxial strain is included in the empirical parameter δ_E—a positive (negative) value indicates a stronger (weaker) exchange interaction between $\mathbf{m}_1$ and $\mathbf{m}_2$.[28,30,31] Therefore, a positive (negative) δ_E corresponds to a shorter (longer) bond length and hence compressive (tensile) strain. The last term in Eq. (1) represents the Zeeman energy due to the externally applied magnetic field $\mathbf{H}_a$. Finally, $\mathbf{u}_{e,i}$ is the local easy axis corresponding to $\mathbf{m}_i$. The easy axes are assumed to be $\mathbf{u}_{e,1} = -(1/2)\mathbf{x} + (\sqrt{3}/2)\mathbf{y}$, $\mathbf{u}_{e,2} = -(1/2)\mathbf{x} - (\sqrt{3}/2)\mathbf{y}$, and $\mathbf{u}_{e,3} = \mathbf{x}$. Mn_3Sn is an exchange dominant AFM such that $J_E \gg D_M \gg K_e$. Typical values of the material parameters of Mn_3Sn, considered in this work, are listed in Table I. The ground states for different δ_E and $\mathbf{H}_a$ can be obtained by minimizing Eq. (1) with respect to $\mathbf{m}_i$.

The ground states of single-domain strained-Mn_3Sn, in the absence of any magnetic field ($\mathbf{H}_a = 0$), are shown in Fig. 2. In all the cases, $\mathbf{m}_1$, $\mathbf{m}_2$, and $\mathbf{m}_3$ exhibit a clockwise ordering with approximately 120° angle between them, all lying within the x–y plane. Compared to the sixfold degeneracy observed in single-domain Mn_3Sn with no strain,[36,38] a twofold spin degeneracy is observed in strained-Mn_3Sn, where $\mathbf{m}_3$ coincides with its easy axis in the case of compressive strain [Figs. 2(a) and 2(b)] while it is perpendicular to its easy axis in the case of tensile strain [Figs. 2(c) and 2(d)].

TABLE I. List of material parameters for the AFM, Mn_3Sn, and the heavy metal (HM), which is chosen as W, in the SOT device setup.

Parameters	Definition	Values	Reference
J_E (J/m^3)	Exchange constant	2.4×10^8	16
D (J/m^3)	DMI constant	2×10^7	16
K_e (J/m^3)	Uniaxial anisotropy constant	3×10^6	16
M_s (A/m)	Saturation magnetization	1.3×10^6	16
$\lvert\delta_E\rvert$	Strain parameter	10^{-3}	30
α	Gilbert damping	0.003	19
θ_{SH}	Spin Hall angle for HM	0.06	30

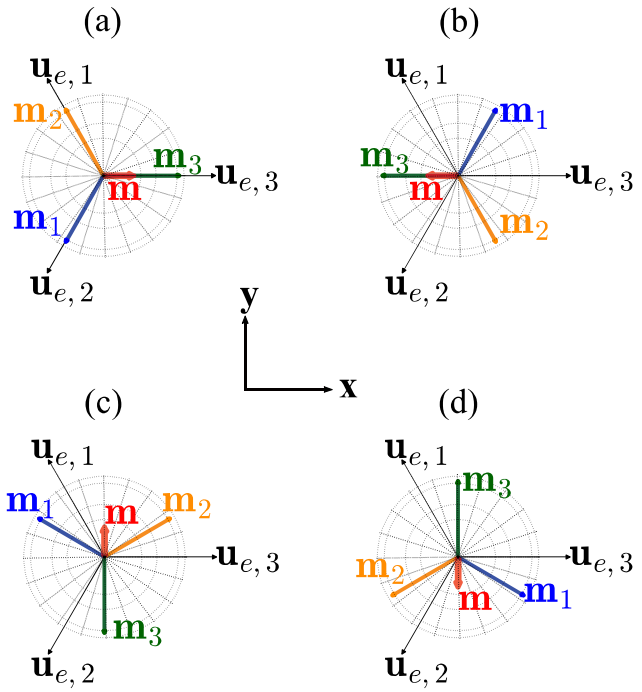

FIG. 2. Equilibrium states in single-domain Mn_3Sn crystal under [(a) and (b)] compressive and [(c) and (d)] tensile strains. The sublattice vectors lie in the Kagome plane, which is assumed to coincide with the x–y plane. [(a) and (b)] Only $\mathbf{m}_3$ coincides with its easy axis. [(c) and (d)] None of the sublattice vectors coincide with their local easy axes. Instead, tensile strain forces $\mathbf{m}_3$ perpendicular to its easy axis. The two equilibrium states for compressive as well as tensile strains are separated by 180° with respect to each other. A small in-(Kagome)-plane average magnetization, $\mathbf{m}$, exists parallel (antiparallel) to $\mathbf{m}_3$ in the case of compressive (tensile) strain. The magnitude of $\mathbf{m}$ depends on the strength of the strain. Here, $\mathbf{m}$ is not drawn to scale but magnified by 100× for the purpose of clear representation.

A small non-zero net magnetization, $\mathbf{m} = \frac{\mathbf{m}_1+\mathbf{m}_2+\mathbf{m}_3}{3}$, exists in single-domain Mn_3Sn with no strain.[36,38] We find that strained-Mn_3Sn also hosts a net magnetization which is parallel (antiparallel) to $\mathbf{m}_3$ in the case of the compressive (tensile) strain. For $|\delta_E| = 10^{-3}$, which represents a uniaxial strain of 0.1%, the norm of the net magnetization increases from the bulk value of $\mathbf{m} \approx 3.66 \times 10^{-3}$ to $\mathbf{m} \approx 3.95 \times 10^{-3}$ ($\mathbf{m} \approx 3.92 \times 10^{-3}$) in the case of compressive (tensile) strain. The non-zero $\mathbf{m}$ suggests that the angle between the sublattice vectors is not exactly 120°. Indeed, in the case of compressive (tensile) strain, $\eta_{12} \approx 0.78°(-0.78°)$ and $\eta_{23} = \eta_{31} \approx -0.39°(0.39°)$, where $\eta_{ij} = \cos^{-1}(\mathbf{m}_i \cdot \mathbf{m}_j) - \frac{2\pi}{3}$. For both compressive and tensile strain, $\eta_{12} + \eta_{23} + \eta_{31} = 0$. For $\delta_E = 0$, our calculations showed that the respective $|\eta_{ij}|$ were different from the values reported above and depended on the ground state under consideration.[36] The aforementioned results with and without strain are as expected—strong exchange and DM interactions attempt enforcing a clockwise ordering of $\mathbf{m}_1$, $\mathbf{m}_2$, and $\mathbf{m}_3$ with exactly 120° angle between them, within a plane perpendicular to the z-axis. However, the

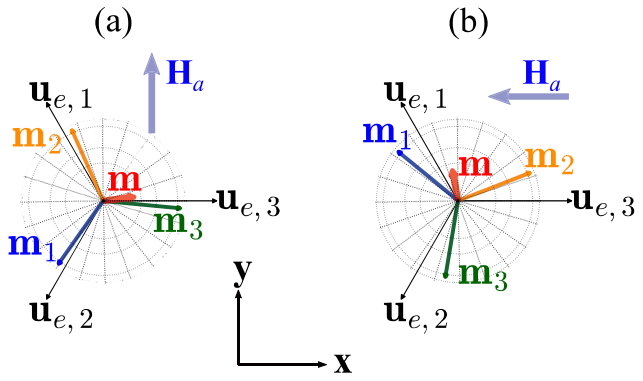

FIG. 3. Ground states of monodomain Mn_3Sn crystal, with (a) compressive strain and (b) tensile strain, under the effect of in-plane external magnetic field, $\mathbf{H}_a = H_0(\cos(\varphi_H), \sin(\varphi_H), 0)$. In both cases, $\mathbf{m}$ tilts toward $\mathbf{H}_a$. Here, $\mathbf{H}_a = 0.1$ T while $\mathbf{m}$ is magnified by 100× for the purpose of clear representation in both cases.

anticlockwise ordering of $\mathbf{u}_{e,1}$, $\mathbf{u}_{e,2}$, and $\mathbf{u}_{e,3}$ forces the sublattice vectors in the x–y plane with a small deviation from the 120° ordering. Uniaxial strain leads to further increase in the deviation.

External magnetic fields, when applied to a thin film of Mn_3Sn, change the energy of the system, and therefore, the ground states. Here, we only consider an external magnetic field in the Kagome plane as $\mathbf{H}_a = H_0(\cos(\varphi_H), \sin(\varphi_H), 0)$, where φ_H is the angle between the magnetic field and the x-axis. Figure 3(a) shows the ground states of Mn_3Sn when $\mathbf{H}_a = (0, 0.1\,\text{T}, 0)$ is applied to the equilibrium state of Fig. 2(a), whereas Fig. 3(b) shows the ground state when $\mathbf{H}_a = (-0.1\,\text{T}, 0, 0)$ is applied to the equilibrium state of Fig. 2(c). In both cases, $\mathbf{m}$ tilts toward the magnetic field, while the sublattice vectors either tilt toward $\mathbf{H}_a$ or away from it, in order to lower the energy of the system. Compared to the equilibrium states of Fig. 2, the angles between the sublattice vectors change, although by a negligible amount. However, if the applied field is large it could disturb the almost 120° relative orientation of the magnetic moments. Therefore, in this work, we consider relatively small magnetic fields that are sufficient to aid the dynamics (discussed later in Sec. III) without disturbing the antiferromagnetic order, viz., $J_E \gg D_M \gg H_0 M_s$.

A. Perturbative analysis

For a clear understanding of the aforementioned ground states of the monodomain strained-Mn_3Sn, we consider the perturbative approach presented in Refs. 38 and 31,39,40. First, we define the sublattice vector as $\mathbf{m}_i = (\sqrt{1-u_i^2}\cos(\varphi_i), \sqrt{1-u_i^2}\sin(\varphi_i), u_i)$, where φ_i and u_i are its azimuthal angle and the z-component, respectively. Second, we define the experimentally relevant cluster magnetic octupole moment[31,40,41] as $\mathbf{m}_{\text{oct}} = \frac{1}{3}\mathcal{M}_{zx}\left[R\left(\frac{2\pi}{3}\right)\mathbf{m}_1 + R\left(-\frac{2\pi}{3}\right)\mathbf{m}_2 + \mathbf{m}_3\right]$. Here, $\mathbf{m}_1$ and $\mathbf{m}_2$ are rotated by $+2\pi/3$ and $-2\pi/3$, respectively, while the y-component of the resultant vector undergoes a mirror operation with respect to the x–z plane.[31,40] This ensures that the octupole and the sublattice vectors are coplanar, and $\varphi_{\text{oct}} = -\frac{\varphi_1+\varphi_2+\varphi_3}{3}$, where φ_{oct} is the azimuthal angle of the magnetic octupole moment. Thirdly, we define $\varphi_i = -\varphi_{\text{oct}} - \frac{2\pi i}{3} + \eta_i$, where η_i is a small angle ($\eta_i \ll 2\pi/3$) that includes the effect of small deviation from the rigid 120° configuration due to both the frustrated bulk structure and the strain. Here, η_i is linearly independent of φ_{oct} and $\eta_1 + \eta_2 + \eta_3 = 0$. Finally, we use the perturbative approach, as outlined in the supplementary material, to arrive at an energy landscape, which is a function of φ_{oct}[31,38–40] and is given as

$$F(\varphi_{\text{oct}}) \approx -\frac{3A}{2}\cos(2\varphi_{\text{oct}}) - \frac{B}{2}\cos(6\varphi_{\text{oct}}) - 3M_sH_0(C\cos(\varphi_{\text{oct}} - \varphi_H) + D\cos(\varphi_{\text{oct}} + \varphi_H)), \quad (2)$$

where $A = \frac{2J_E\delta_E K_e}{3(J_E+\sqrt{3}D_M)}$, $B = \frac{(3J_E+7\sqrt{3}D_M)K_e^3}{9(J_E+\sqrt{3}D_M)^3}$, $C = \frac{K_e}{3(J_E+\sqrt{3}D_M)}$, and $D = \frac{J_E\delta_E}{3(J_E+\sqrt{3}D_M)}$. The constant terms are not shown here as they do not affect the ground states solution.

For $H_0 = 0$ in Eq. (2), the $\cos(2\varphi_{\text{oct}})$ term dominates over the $\cos(6\varphi_{\text{oct}})$ term, if $A \gg B$ and $|A| \gg 3B$ in the case of Mn_3Sn with compressive and tensile strains, respectively. For the material parameters listed in Table I, these conditions are equivalent to $\delta_E \gg 0.08 \times 10^{-3}$ and $|\delta_E| \gg 0.24 \times 10^{-3}$, respectively. Therefore, for $|\delta_E| = 10^{-3}$, compressive (tensile) strain leads to two minimum energy equilibrium states of the octupole moment, corresponding to $\varphi_{\text{oct}} = 0$ and π ($\varphi_{\text{oct}} = \pi/2$ and $3\pi/2$), as shown in Fig. 2. On the other hand, when a magnetic field is turned on ($H_0 > 0$), the energy of the system changes, and two ground states of the octupole moment, corresponding to the minimum of Eq. (2), are possible. We find that, if φ_H is 0° or 180° (90° or 270°) for Mn_3Sn with compressive (tensile) strain, the possible ground states are the same as the initial equilibrium states. Conversely, if φ_H is different from the equilibrium direction, the possible ground states are different from the equilibrium states (Fig. 3).

In the special case of $\mathbf{H}_a$ perpendicular to the equilibrium direction, degenerate ground states with energies lower than that of

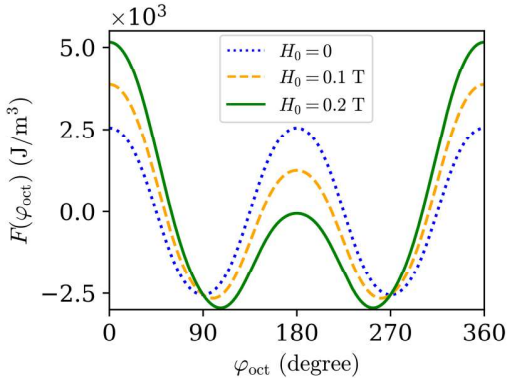

FIG. 4. Energy density as a function of the octupole angle of a monodomain Mn_3Sn with tensile strain for different applied magnetic field, H_0, along the −x-direction ($\varphi_H = 180°$). External magnetic field breaks the symmetry of the system, and, therefore, the barrier height reduces at $\varphi_{\text{oct}} = \pi$ but increases at $\varphi_{\text{oct}} = 0$, as H_0 increases.

the equilibrium states are obtained. This is depicted in Fig. 4, where an external magnetic field is applied in the negative x-direction ($\varphi_H = 180°$) to Mn_3Sn with tensile strain. As the strength of the magnetic field increases, the energy of the ground states decrease and they move away from the equilibrium states of 90° and 270°, toward 180°. In addition, the energy barrier separating the two states reduces at 180° but increases at 360°. The two ground states exist if $H_0 \lesssim \frac{2|A+3B|}{M_s(C+D)}$. Within this limit, $\mathbf{m}$ was found to increase with both δ_E and H_0 (see the supplementary material). For higher H_0, $\varphi_{oct} = \pi$ becomes a minimum too and $\mathbf{m}$ decreases with δ_E at fixed H_0 (supplementary material). In the case of Mn_3Sn with compressive strain and $\mathbf{H}_a$ perpendicular to the equilibrium states, two ground states exist if $H_0 \lesssim \frac{2(A+3B)}{M_s(C-D)}$. These limits suggest that the maximum value of H_0, which could be applied while maintaining two ground states, increases with δ_E. This is because larger δ_E leads to higher intrinsic energy barrier, which is given as $|3A + B|$, between the two equilibrium states.

III. SOT-DRIVEN DYNAMICS

To investigate the dynamics of Mn_3Sn under the effect of spin current, we consider the spin-Hall effect (SHE) setup shown in Fig. 5. This setup resembles the experimental designs from Refs. 30 and 31, where Mn_3Sn grown epitaxially on a (110)[001] MgO substrate exhibits uniaxial tensile strain in the x-direction resulting in a PMA energy landscape for the magnetic octupole moment.[30,31] Hereafter, we only focus on the dynamics of single-domain Mn_3Sn with tensile strain while the discussion on the dynamics of Mn_3Sn with compressive strain and no strain is relegated to the supplementary material. In our convention, as mentioned previously, the Kagome plane of Mn_3Sn is assumed to coincide with the x–y plane, while the z-axis coincides with the [0001] direction. Charge-to-spin conversion in the HM, due to the flow of charge current density, J_c, leads to the generation of a spin current density, J_s, polarized along $\mathbf{n}_p$, which is assumed to coincide with the z-axis. Previous works have shown that the current required to induce dynamics in this setup, with $\mathbf{n}_p$ perpendicular to the Kagome plane, is significantly smaller than that required in the case where $\mathbf{n}_p$ is parallel to the Kagome plane.[20,30,31] Finally, the external field $\mathbf{H}_a$ is assumed to be applied in the negative x-direction, or $\varphi_H = 180°$.

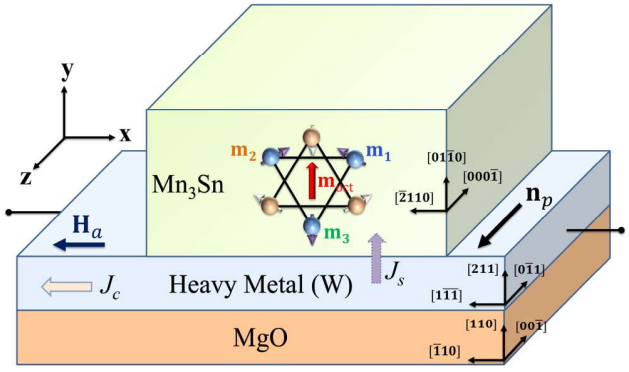

FIG. 5. Spin–orbit torque device setup for manipulating the magnetic state in Mn_3Sn. The MgO substrate leads to tensile strain in the x-direction, and hence, the PMA in Mn_3Sn. Spin-Hall effect in the HM generates SOT when a charge current flows into it. J_c and J_s are the charge current density and the spin current density, respectively. $\mathbf{H}_a$ is the external magnetic field, which is applied to aid the deterministic switching of the magnetic octupole moment, $\mathbf{m}_{oct}$, in strained-Mn_3Sn.

For each sublattice of Mn_3Sn, the magnetization dynamics is governed by the classical Landau–Lifshitz–Gilbert (LLG) equation, which is a statement of the conservation of angular momentum. The LLG equations for the three sub-lattices are coupled via the exchange interactions.[16,35] For sublattice i, the LLG equation is given as[42]

$$\dot{\mathbf{m}}_i = -\gamma(\mathbf{m}_i \times \mathbf{H}_i^{\text{eff}}) + \alpha(\mathbf{m}_i \times \dot{\mathbf{m}}_i) - \frac{\hbar}{2e}\frac{\gamma J_s}{M_s d_a}\mathbf{m}_i \times (\mathbf{m}_i \times \mathbf{n}_p), \tag{3}$$

where $\dot{\mathbf{m}}_i = \frac{\partial \mathbf{m}_i}{\partial t}$, t is time in seconds, $\mathbf{H}_i^{\text{eff}}$ is the effective magnetic field experienced by $\mathbf{m}_i$, α is the Gilbert damping parameter for Mn_3Sn, and d_a is the thickness of the AFM layer. Other parameters in this equation, viz., $\hbar = 1.054\,561 \times 10^{-34}$ J s, $e = 1.6 \times 10^{-19}$ C, and $\gamma = 17.6 \times 10^{10}\,\text{T}^{-1}\,\text{s}^{-1}$ are the reduced Planck constant, the elementary charge of an electron, and the gyromagnetic ratio, respectively. The spin current density depends on the input charge current density and the spin-Hall angle of the HM, θ_{SH}, as $J_s = \theta_{SH} J_c$. The spin-Hall angle is associated with the efficiency of the SOT effect. Here, we consider the HM to be W since it has a large θ_{SH}.[19]

The effective magnetic field for sublattice i can be obtained by using Eq. (1) as

$$\mathbf{H}_i^{\text{eff}} = -\frac{1}{M_s}\frac{\partial F}{\partial \mathbf{m}_i} = -\frac{J_E}{M_s}(\mathbf{m}_j + \mathbf{m}_k) + \frac{D_M \mathbf{z} \times (\mathbf{m}_j - \mathbf{m}_k)}{M_s} + \frac{2K_e}{M_s}(\mathbf{m}_i \cdot \mathbf{u}_{e,i})\mathbf{u}_{e,i} + \mathbf{H}_a, \tag{4}$$

where $(i, j, k) = (1, 2, 3), (2, 3, 1),$ or $(3, 1, 2)$, respectively. Equations (3) and (4) are then solved simultaneously for a range of $H_0(>0)$ and J_s, for both $\varphi_{oct}^{init} = \pi/2$ and $\varphi_{oct}^{init} = 3\pi/2$ as the initial states. The steady-state response of the magnetic order of Mn_3Sn is found to be dependent on the initial ground states, magnitude of H_0, and the direction and magnitude of the input current. These differences in the steady state behavior are shown in Figs. 6 and 7 for $H_0 = 0.1$ T and $\varphi_H = 180°$.

Figure 6 shows the time dynamics of the magnetic octupole moment and that of the out-of-(Kagome)-plane component of the average magnetization, m_z, for the current pulse shown in Fig. 6(b). It can be observed that for $t < 1$ ns, where $J_s = 0$, the magnetic octupole moment evolves to ground states (i) and (ii), for the equilibrium states at $\varphi_{oct}^{init} = \pi/2$ and $\varphi_{oct}^{init} = 3\pi/2$, respectively. When J_s is increased to 1.5 MA/cm^2 at $t = 1$ ns, (i) and (ii) evolve to stationary steady states (iii) and (iv), respectively. Although the φ_{oct} corresponding to both (iii) and (iv) are larger than those for (i)

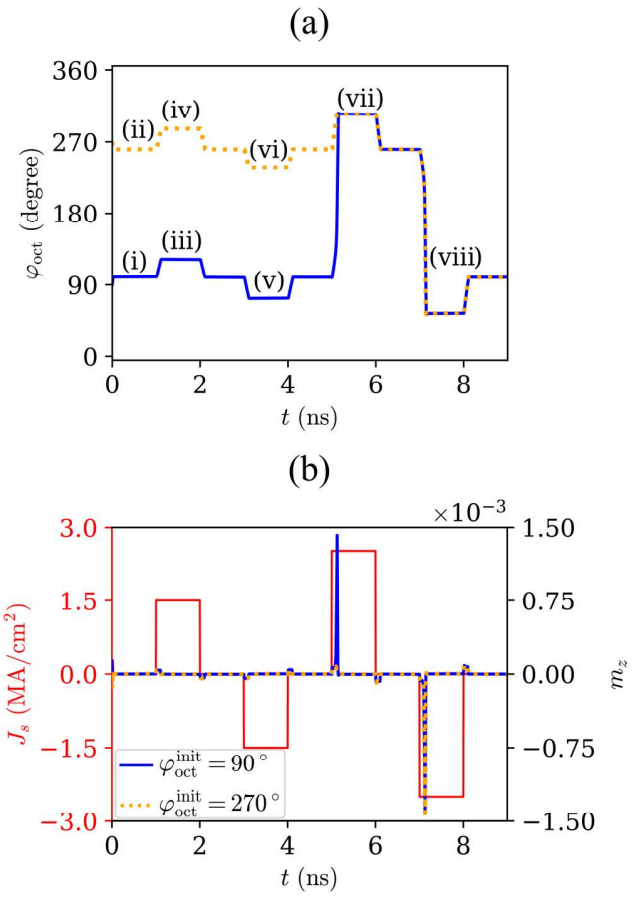

FIG. 6. Steady-state response of (a) the magnetic octupole moment and (b) the out-of-(Kagome)-plane component of the average magnetization, m_z, as a function of time under the effect of a current pulse, which is turned on at $t = 1$ ns and $t = 3$ ns to $|J_s| = 1.5\,\mathrm{MA/cm^2}$, while it is increased to $|J_s| = 2.5\,\mathrm{MA/cm^2}$ at $t = 5$ ns and $t = 7$ ns. Otherwise, the current is turned off. (a) (i) and (ii): Possible ground states for $H_0 = 0.1$ T in the negative x-direction and $J_s = 0$. (iii) and (iv): $J_s = 1.5\,\mathrm{MA/cm^2}$. No switching. Stationary states at angles larger than (i) and (ii), respectively. (v) and (vi): $J_s = -1.5\,\mathrm{MA/cm^2}$. No switching. Stationary states at angles smaller than (i) and (ii), respectively. (vii): $J_s = 2.5\,\mathrm{MA/cm^2}$. Deterministic switching of (i). No switching for (ii). Stationary states at angles larger than (ii). (viii): $J_s = -2.5\,\mathrm{MA/cm^2}$. Deterministic switching of (ii). Stationary states at angles smaller than (i). (b) $|m_z|$ is zero in the steady state but increases during the switching process. The change in $|m_z|$ is negligible for the case of no switching.

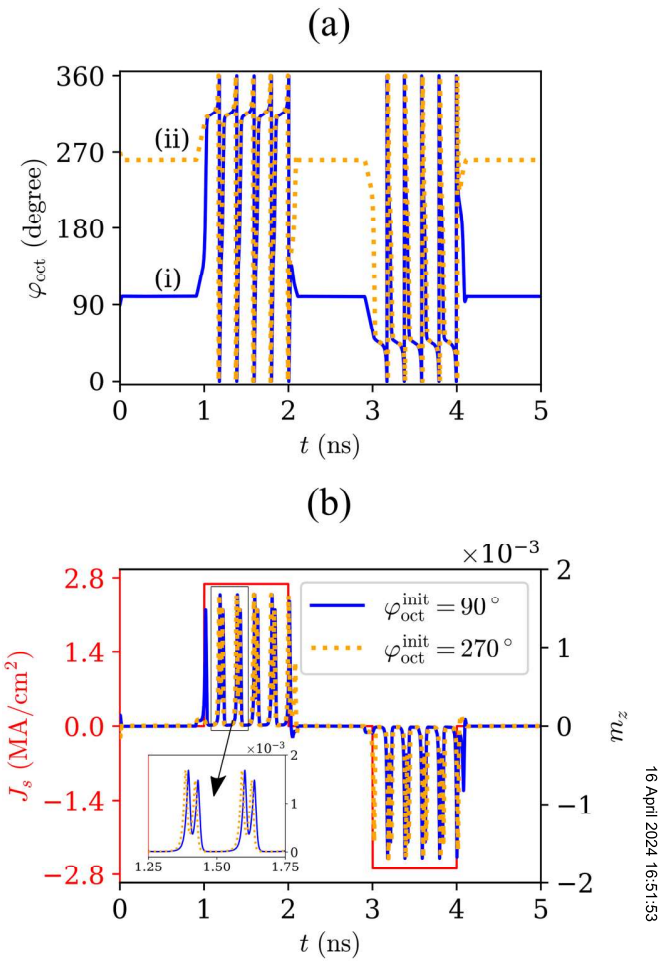

FIG. 7. Steady-state oscillation dynamics of (a) the magnetic octupole moment and (b) the out-of-(Kagome)-plane component of the average magnetization, m_z, as a function of time under the effect of a current pulse. The pulse is turned on at $t = 1$ ns ($t = 3$ ns) to $J_s = 2.69\,\mathrm{MA/cm^2}$ ($J_s = -2.69\,\mathrm{MA/cm^2}$) and turned off at $t = 2$ ns ($t = 4$ ns). (a) (i) and (ii): Possible ground states for $H_0 = 0.1$ T in the negative x-direction. Oscillation dynamics for $|J_s| = 2.69\,\mathrm{MA/cm^2}$: the octupole moment in both (i) and (ii) oscillate at a frequency of about 2.5 GHz in a direction decided by the direction of the input current. When the current is turned off, the octupole moment probabilistically settles into either of (i) or (ii). (b) Non-zero m_z facilitates high frequency chiral oscillations in the steady state due to the strong exchange interaction between out-of-(Kagome)-plane components of the sublattice vectors.

and (ii), they are still near the initial states, that is, $1.5\,\mathrm{MA/cm^2}$ is not large enough to induce deterministic switching. Stationary steady states near the initial ground states are also observed when J_s is decreased to $-1.5\,\mathrm{MA/cm^2}$ at $t = 3$ ns: (i) and (ii) evolve to (v) and (vi), respectively. In this case, the $\varphi_{\rm oct}$ corresponding to the stationary states are smaller than those of the ground states. States (iii) and (v) return to the ground state (i) while (iv) and (vi) return to the ground state (ii), when the current is turned off. The final steady states, therefore, depend on both the magnitude and the direction of the input current. As shown in Fig. 6(b), m_z is zero in the steady state. It changes negligibly, in the direction of the change in J_s, when the current is turned on or off.

It can be further observed from Fig. 6(a) that the magnetic octupole moment in both ground states (i) and (ii) evolve to the stationary steady state (vii), when J_s is increased to $2.5\,\mathrm{MA/cm^2}$ at $t = 5$ ns. On the one hand, this dynamics corresponds to the

deterministic switching of the magnetic octupole moment in (i). On the other hand, for the magnetic octupole moment in (ii), (vii) is just a stationary steady state with φ_{oct} greater than that of (ii). However, when the current direction is reversed by lowering J_s to $-2.5\,\mathrm{MA/cm^2}$ at $t = 7\,\mathrm{ns}$, the magnetic octupole moment in (ii) switches deterministically to (viii), which is near (i) but has a smaller corresponding φ_{oct}. In this case, the magnetic octupole moment in (i) will not switch, but move to (viii). As shown in Fig. 6(b) at $t = 5\,\mathrm{ns}$ and $t = 7\,\mathrm{ns}$, deterministic switching is accompanied by a large spike in m_z. The direction of change in m_z depends on the direction of the input current—positive (negative) J_s leads to positive (negative) m_z.

Further increasing $|J_s|$ to $2.69\,\mathrm{MA/cm^2}$ results in chiral oscillations for the magnetic octupole moment in both ground states (i) and (ii), as shown in Fig. 7(a). For positive J_s, the magnetic octupole moment in (i) deterministically switches to (ii) in the first step; therefore, the phase of (i) lags that of (ii). On the contrary, for negative J_s, the magnetic octupole moment in (ii) deterministically switch to (i) in the first step; therefore, the phase of (ii) lags that of (i). The oscillation dynamics of the magnetic octupole moment is accompanied by large m_z, as shown in Fig. 7(b). Similar to the case of deterministic switching dynamics, the direction of m_z depends on the direction of current—positive (negative) J_s leads to positive (negative) m_z. However, unlike the case of deterministic switching, m_z shows two spikes per oscillation [inset of Fig. 7(b)].

Detailed numerical simulations revealed that for $\varphi_{oct}^{init} = \pi/2$ ($\varphi_{oct}^{init} = 3\pi/2$) and $J_s > 0$ ($J_s < 0$), the final steady state of $\mathbf{m}_{oct}$ depended on the magnitude of J_s with respect to two threshold currents—J_s^{th1} and J_s^{th2}, where $J_s^{th1} < J_s^{th2}$. As summarized in Fig. 8, if the injected current density is smaller than the lower threshold current, that is, $|J_s| < J_s^{th1}$, the ground state of the AFM evolves to a non-equilibrium stationary steady state in the initial energy well.

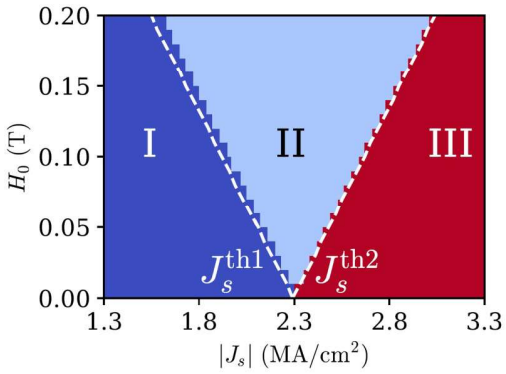

FIG. 8. Final steady state as a function of the magnitude of the input current, $|J_s|$, for different applied magnetic fields H_0. I, II, and III represent regions of no switching, switching, and chiral oscillation, respectively. The dashed white lines represent the two threshold currents, J_s^{th1} and J_s^{th2} obtained from numerical solution of Eq. (6). This phase diagram is applicable if $\varphi_{oct}^{init} = \pi/2$ ($\varphi_{oct}^{init} = 3\pi/2$) and $J_s > 0$ ($J_s < 0$). For $\varphi_{oct}^{init} = 3\pi/2$ ($\varphi_{oct}^{init} = \pi/2$) and $J_s > 0$ ($J_s < 0$), region III would still represent chiral oscillation, however, the regions encompassing I and II would both correspond to no switching.

The case of $|J_s| = 1.5\,\mathrm{MA/cm^2}$ and $H_0 = 0.1\,\mathrm{T}$, shown in Fig. 6(a), belongs to this regime. On the other hand, if $J_s^{th1} < |J_s| < J_s^{th2}$, the magnetic octupole moment deterministically switches to a non-equilibrium stationary steady state in the other energy well [$|J_s| = 2.5\,\mathrm{MA/cm^2}$ and $H_0 = 0.1\,\mathrm{T}$ in Fig. 6(a)]. Finally, when $J_s^{th2} < |J_s|$, the magnetic octupole moment exhibits steady-state chiral oscillations [$|J_s| = 2.69\,\mathrm{MA/cm^2}$ and $H_0 = 0.1\,\mathrm{T}$ in Fig. 7(a)], whose frequency could be tuned from the 100s of MHz to the 10s of GHz range by varying $|J_s|$. The three regimes of operation are marked as I, II, and III for no switching, deterministic switching, and chiral-rotation, respectively. The overlaid dashed white lines represent J_s^{th1} and J_s^{th2}. It can be observed that J_s^{th1} decreases with an increase in H_0 while J_s^{th2} increases with H_0. As a result, the range of input currents where the system exhibits deterministic switching increases with H_0. For $\varphi_{oct}^{init} = 3\pi/2$ ($\varphi_{oct}^{init} = \pi/2$) and $J_s > 0$ ($J_s < 0$), the magnetic octupole moment displays a stationary steady state in the initial energy well, if $|J_s| < J_s^{th2}$ [Fig. 6(a)], while it shows chiral oscillations for $J_s^{th2} < |J_s|$ [Fig. 7(a)]. In the limiting case of $H_0 = 0$, $J_s^{th1} = J_s^{th2}$, and no deterministic switching of the magnetic octupole moment is observed. Instead, the magnetic octupole moment displays either a non-equilibrium stationary state in the initial energy well or chiral oscillations. If the current is turned off during the oscillation, the magnetic octupole moment probabilistically switches to either of the energy wells.[20,29,36]

A. Stationary state and threshold current

To explore the dependence of the dynamics on the intrinsic energy scale of the system, obtain analytic expressions for the two threshold currents as a function of the applied magnetic field and material parameters, and establish scaling laws related to switching and chiral oscillations, we evaluate the rate of change of the average magnetization, $\dot{\mathbf{m}} = \frac{(\dot{\mathbf{m}}_1+\dot{\mathbf{m}}_2+\dot{\mathbf{m}}_3)}{3}$, as

$$\dot{\mathbf{m}} = \frac{1}{3}\sum_{i=1}^{3}\Big(-\gamma(\mathbf{m}_i \times \mathbf{H}_i^{\mathrm{eff}}) + \alpha(\mathbf{m}_i \times \dot{\mathbf{m}}_i). \\ -\frac{\hbar}{2e}\frac{\gamma J_s}{M_s d_a}(\mathbf{m}_i \times (\mathbf{m}_i \times \mathbf{z}))\Big), \tag{5}$$

where $\mathbf{m}_i \times \mathbf{H}_i^{\mathrm{eff}} = \frac{1}{3\mu_0 M_s}\frac{\partial F}{\partial \varphi_{oct}}\mathbf{z}$ while $\frac{\partial F}{\partial \varphi_{oct}}$ is obtained from Eq. (2) with $\varphi_H = \pi$.

In the stationary states, irrespective of φ_{oct}^{init}, the net torque on the magnetic octupole moment is zero since the spin–orbit torque generated by the input current is balanced by the torque due to the internal and external magnetic fields. Consequently, we set the time derivatives ($\dot{\mathbf{m}}$ and $\dot{\mathbf{m}}_i$) in Eq. (5) to zero. Our numerical simulations revealed that the z-component of all the sublattice vectors were zero in the stationary steady state. So, we set $m_{i,z} = u_i = 0$ in Eq. (5) to arrive at the torque balance equation

$$A\sin(2\varphi_{oct}) + B\sin(6\varphi_{oct}) - M_s H_0(C+D)\sin(\varphi_{oct}) = \frac{\hbar}{2e}\frac{J_s}{d_a}. \tag{6}$$

For $\varphi_{oct}^{init} = \pi/2$ and $0 \le J_s < J_s^{th1}$, the solution to Eq. (6) should lead to one stationary solution with $\mathrm{GS}_1 \le \varphi_{oct} < \pi$, where $\mathrm{GS}_1 \in (\pi/2, \pi)$ is the smaller of the two minima of Eq. (2). On the other hand, for $J_s^{th1} \le J_s < J_s^{th2}$, the magnetic octupole moment

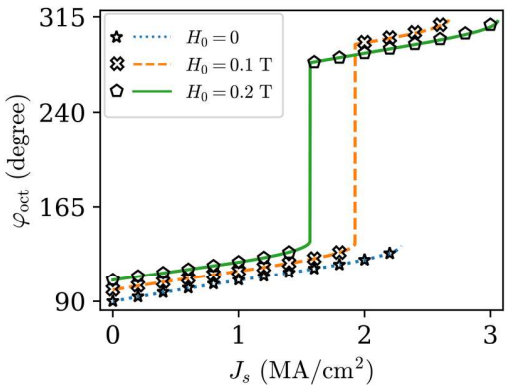

FIG. 9. Stationary steady states as a function of the applied spin current, J_s, for a thin film of Mn_3Sn under tensile strain. Numerical result from the solution of Eq. (3) (symbols) agree very well with the results obtained from Eq. (6) (lines).

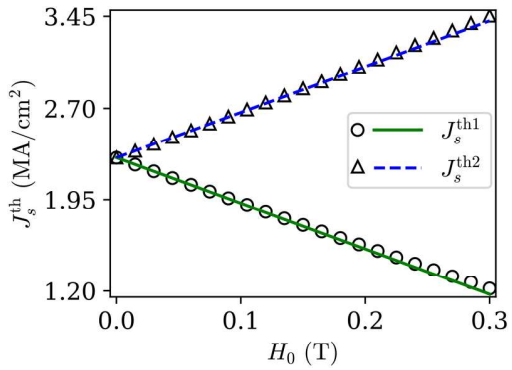

FIG. 10. Comparison of the analytic expressions of threshold currents [Eq. (7)], shown by lines, against the numerical values obtained from the solution of Eq. (6), represented by symbols. The numerical and analytic values show excellent agreement for the values of H_0 considered here.

should switch to a stationary state in the other energy well, and the solution of Eq. (6) should lead to $GS_2 < \varphi_{oct} < 2\pi$. Here, $GS_2 \in (\pi, 3\pi/2)$ is the larger of the two minima of Eq. (2). Indeed the same can be observed from Fig. 9, where the numerical solutions of the coupled LLG equations (symbols) fit the solutions from Eq. (6) (lines) very well in both energy wells, for three different values of H_0. Consequently, J_s^{th1} is the minimum current for which Eq. (6) has no solution in (GS_1, π), but has a solution in $(GS_2, 2\pi)$. On the other hand, J_s^{th2} is the minimum current for which Eq. (6) has no solutions. The numerical solution of the threshold currents for different H_0, obtained from Eq. (6), is shown by the dashed white lines overlaid on Fig. 8. It can be observed that the solutions from Eq. (6) match the results from Eq. (3) very well. If $\varphi_{oct}^{init} = 3\pi/2$ and $0 \le J_s < J_s^{th2}$, the solution of Eq. (6) would lead to $GS_2 \le \varphi_{oct} < 2\pi$, as is shown in Fig. 9 for $J_s^{th1} \le J_s < J_s^{th2}$. Although not shown here, reversing the direction of current ($J_s < 0$) with $0 \le |J_s| < J_s^{th2}$ leads to stationary steady states in $(0, GS_1]$ for $\varphi_{oct}^{init} = \pi/2$ while $\varphi_{oct}^{init} = 3\pi/2$ exhibits a stationary state in $(\pi, GS_2]$, if $0 \le |J_s| < J_s^{th1}$, and in $(0, GS_1)$, if $J_s^{th1} \le |J_s| < J_s^{th2}$.

An exact expression of either of the two threshold currents is cumbersome to obtain, however, in the limit of small magnetic fields that do not disturb the twofold degeneracy of PMA Mn_3Sn, they can be approximated as

$$J_s^{th1} = d_a \frac{2e}{\hbar}\left(-A + B - \frac{M_s H_0}{\sqrt{2}}(C + D)\right), \tag{7a}$$

$$J_s^{th2} = d_a \frac{2e}{\hbar}\left(-A + B + \frac{M_s H_0}{\sqrt{2}}(C + D)\right). \tag{7b}$$

In the absence of an external magnetic field, the threshold current is the minimum current that provides just enough SOT to overcome the maximum torque due to the effective in-plane anisotropy. This maximum occurs at $\varphi_{oct} = 45°$, 135°, 225°, and 315° since they lead to $\sin(2\varphi_{oct}) = \pm 1$ and $\sin(6\varphi_{oct}) = \mp 1$. For non-zero external magnetic field, first, we consider the effect of the in-plane anisotropy to be dominant while that of H_0 to be small. We then evaluate Eq. (6) at $\varphi_{oct} = 135°$ and $\varphi_{oct} = 315°$ to obtain J_s^{th1} and J_s^{th2}, respectively. Figure 10 compares the analytic expressions of Eq. (7) (lines) against the values of the threshold currents obtained from the solution of Eq. (6) (symbols), for different values of H_0. It can be observed that the analytic results match very well against the numerical values. Since the torque due to H_0 acts against (along) the torque due to the effective in-plane anisotropy at $\varphi_{oct} = 135°$ ($\varphi_{oct} = 315°$), larger H_0 reduces (increases) J_s^{th1} (J_s^{th2}). Although the error between the numerical and the analytic values of the two threshold currents increases with an increase in H_0, it is still smaller than 5% even for $H_0 = 0.3$ T. This linear dependence of the threshold currents on the external field is similar to that in the case of a PMA ferromagnet driven by a SOT.[43]

B. Deterministic switching dynamics

For $H_0 > 0$ and $J_s^{th1} \le |J_s| < J_s^{th2}$, the time derivatives in Eq. (5) change to non-zero values ($|\dot{\mathbf{m}}| > 0$ and $|\dot{\mathbf{m}}_i| > 0$), if $\varphi_{oct}^{int} = 90°$ ($\varphi_{oct}^{int} = 270°$) and $J_s > 0$ ($J_s < 0$). Here, the external magnetic field assists the SOT in overcoming the maximum torque due to the internal magnetic fields. Consequently, the magnetic octupole moment moves away from its initial stable state and switches over the energy barrier at $\varphi_{oct} = 180°$ to the other energy well, while both $|m_z|$ and $|u_i|$ increase to non-zero values. In the second energy well, initially, the torque due to the magnetic fields and the SOT act in the same direction, leading to further increase in $|m_z|$ until $\dot{\mathbf{m}}$ decreases to zero due to the effect of the intrinsic damping. Subsequently, $|m_z|$ decreases to zero while the octupole moment slows down and reaches a stationary state. The SOT cannot overcome the torques due to the magnetic fields anymore since the external field aids the internal fields in the second energy well. If, however, the input current is reversed, such that $J_s^{th1} \le |J_s| < J_s^{th2}$, for the same H_0, the magnetic octupole moment goes back to the initial energy well, by crossing the barrier at

$\varphi_{oct} = 180^\circ$ as the external field assists the SOT. This bidirectional switching behavior was clearly demonstrated in Fig. 6 for $|J_s| = 2.5\,\mathrm{MA/cm^2}$ and $H_0 = 0.1\,\mathrm{T}$. Instead of reversing J_s, if $\mathbf{H}_a$ was reversed to the positive x-direction, the deterministic switching dynamics would have proceeded by crossing the barrier at $\varphi_{oct} = 360^\circ$, provided that $J_s^{th1} \leq |J_s| < J_s^{th2}$.

The SOT-driven bidirectional deterministic switching dynamics in PMA Mn_3Sn could be useful for building next-generation antiferromagnetic memory devices. In this regard, the switching time, t_{sw}, as a function of the input current is an important metric. Figure 11 shows the t_{sw} as function of J_s for two different magnetic fields. Here, t_{sw} is defined as the time taken by the magnetic octupole moment in the ground state $\varphi_{oct}^{init} = \pi/2$ to go from $\varphi_{oct} = \pi/2$ to $\varphi_{oct} = \pi$. This is the minimum duration of an input current pulse that can induce deterministic switching. Such a pulse ensures that the magnetic octupole moment reaches the top of the energy barrier. Thereafter, the current pulse is turned off and the torques due to the magnetic fields assist in switching to the other energy well. It can be observed from Fig. 11 that t_{sw} decreases with an increase in either J_s or H_0. For a fixed H_0, t_{sw} decreases with an increase in J_s since a higher input current leads to a larger SOT on the magnetic octupole moment. On the other hand, at a fixed J_s, t_{sw} decreases with an increase in H_0 since it lowers the energy barrier at $\varphi_{oct} = 180^\circ$, as shown in Fig. 4.

Our numerical simulations showed that both u_i and m_z were relatively small as the magnetic octupole moved from $\varphi_{oct} = \pi/2$ to $\varphi_{oct} = \pi$. Therefore, the switching time was obtained from the z-component of Eq. (5) as

$$t_{sw} = \frac{\alpha M_s}{\gamma}\frac{2e}{\hbar}\frac{d_a}{J_s}\int_{\pi/2}^{\pi} \times \frac{d\varphi_{oct}^{'}}{1 - \frac{(A\sin(2\varphi_{oct}^{'}) + B\sin(6\varphi_{oct}^{'}) - M_s H_0 (C+D)\sin(\varphi_{oct}^{'}))}{\frac{\hbar J_s}{2ed_a}}}, \tag{8}$$

where we neglected the rate of change of m_z since $\frac{\partial m_z}{\partial t} \ll \alpha \frac{\partial \varphi_{oct}}{\partial t}$. It can be observed from Fig. 11 that the switching times obtained from the numerical integration of Eq. (8) (lines) fit the data obtained from the solution of Eq. (3) (symbols) very well for the two magnetic fields considered here.

C. Oscillation dynamics

For $H_0 > 0$ and $J_s^{th2} \leq |J_s|$, the SOT overcomes the maximum of the torques due to the internal and external magnetic fields, irrespective of the initial state or the direction of input current, resulting in $|\dot{\mathbf{m}}| > 0$ and $|\dot{\mathbf{m}}_i| > 0$. Consequently, the magnetic octupole moves away from its initial stable state, crosses the barrier at $\varphi_{oct} = 360^\circ$, and oscillates between the two energy wells with frequencies ranging between 100s of MHz to 10s of GHz, as shown in Fig. 12. Similar to the case of deterministic switching dynamics, $|m_z|$ increases till $\dot{\mathbf{m}}$ reaches zero due to the intrinsic damping, following which $|m_z|$ decreases. Here, however, $|m_z|$ increases again as $\dot{\mathbf{m}}$ increases, owing to the different direction of the torques in each energy well. Therefore, m_z exhibits two peaks of varying magnitude in each oscillation cycle, as shown clearly in the inset of Fig. 7(b). The higher peak occurs after the octupole moment crosses the energy barrier at $\varphi_{oct} = 360^\circ$, whereas the lower peak occurs after it crosses the energy barrier at $\varphi_{oct} = 180^\circ$.

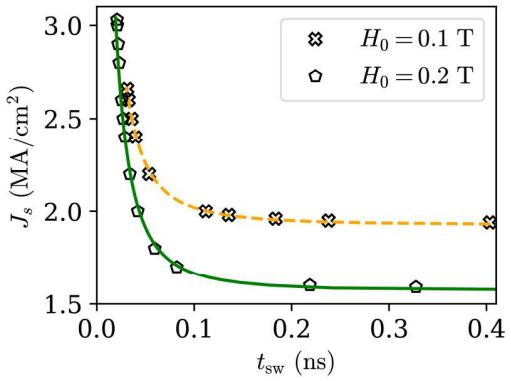

FIG. 11. Switching time, t_{sw}, as a function of the applied spin current, J_s, and external magnetic field, H_0, for a thin film of Mn_3Sn under tensile strain. In each case, the applied current is above J_s^{th1} and below J_s^{th2}. t_{sw} obtained from the solution of Eq. (8) (lines) fits the data obtained from the solution of Eq. (3) (symbols) very well.

For medium to large currents, the oscillation frequency, f, is almost independent of H_0 and increases linearly with J_s, as shown in Fig. 12. The dashed-dotted red line, which corresponds to $f = \frac{\gamma}{2\pi\alpha M_s}\frac{\hbar}{2e}\frac{J_s}{d_a}$, represents this behavior clearly. For such J_s, u_i increases to larger values. Consequently, the effect of the out-of-(Kagome)-plane exchange interaction on the dynamics is expected to become significant while that of the in-plane anisotropy and H_0 is expected to reduce. The x- and z-components of $\mathbf{m}$ as functions of time, for $J_s = 8\,\mathrm{MA/cm^2}$ and three different magnetic fields, are shown in Fig. 13. Although the average frequency

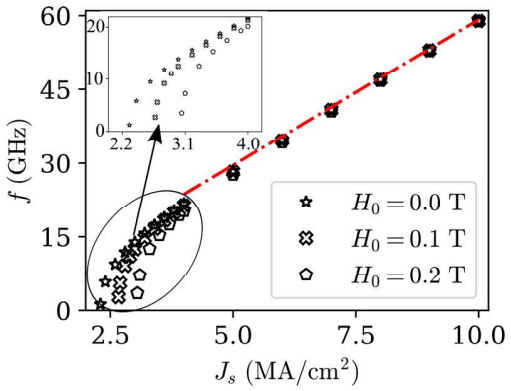

FIG. 12. Oscillation frequency as a function of the applied spin current, J_s, and external magnetic field, H_0, for a thin film of Mn_3Sn under tensile strain. In each case, the applied current is above the respective J_s^{th2}. The dashed-dotted red line represents $f = \frac{\gamma}{2\pi\alpha M_s}\frac{\hbar}{2e}\frac{J_s}{d_a}$ and fits the numerical data very well for large J_s. The figure in the inset shows the variation in f with J_s for smaller input currents.

in the three cases is the same, there are subtle differences in the magnetization dynamics, owing to the symmetry-breaking magnetic field. In particular, m_z is symmetric only for $H_0 = 0$ while it shows the expected asymmetry for non-zero H_0. Since the difference between the barrier heights increases with an increase in H_0 (Fig. 4), the asymmetry in m_z is more prominent for $H_0 = 0.2$ T. A small asymmetry can also be observed in the sinusoidal m_x, where the magnitude in the negative (positive) x-direction increases (decreases) with H_0, owing to $\mathbf{H}_a$ being along the negative x-direction. Although not shown here, non-zero magnetic fields have negligible effect on the y-component of **m**.

For small currents, on the other hand, Fig. 12 shows that f increases non-linearly with J_s and depends on H_0. This dependence of the oscillation dynamics on magnetic fields can also be observed from Fig. 14, which shows the dynamics of m_x and m_z for three different magnetic fields near their respective threshold currents. The strong in-plane anisotropy leads to non-sinusoidal m_x, unlike

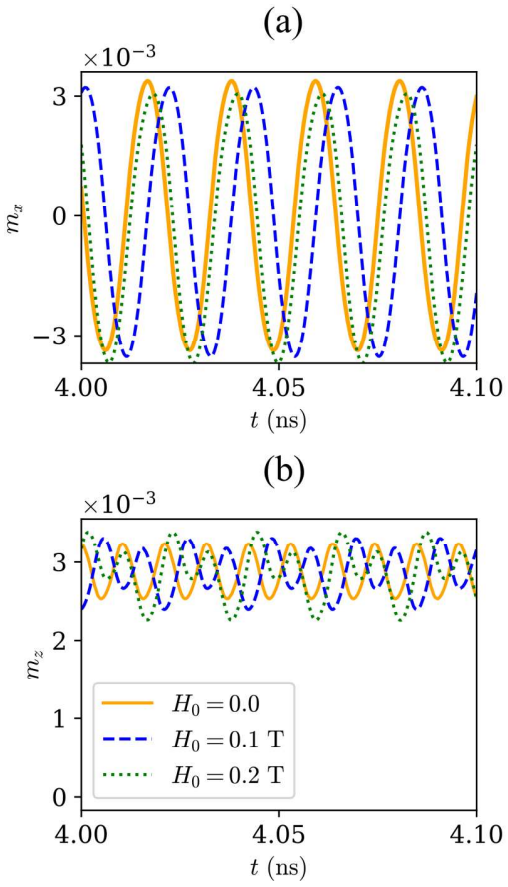

FIG. 13. (a) The x-component and (b) z-component of the average magnetization vector, **m**, as functions of time, for large current $J_s = 8\,\mathrm{MA/cm^2}$ and three different values of H_0. Although the average oscillation frequency is evaluated to be the same for such large current, both m_x and m_z show the effect of H_0.

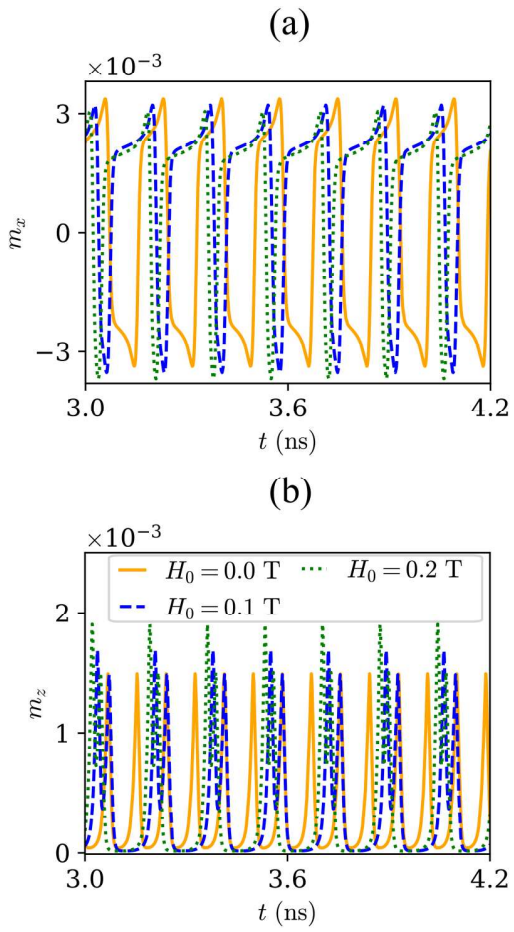

FIG. 14. (a) The x-component and (b) z-component of the average magnetization vector as functions of time at small current ($J_s \simeq J_s^{th2}$) for two different values of H_0. The effect of the in-plane effective anisotropy is evident from the shape of m_x. For non-zero H_0, the m_z shows two spikes of varying amplitude due to energy barriers of different heights.

the case of large J_s [Fig. 13(a)]. It also leads to a spike-like dynamics of m_z, where each oscillation of the magnetic octupole moment is accompanied by two spikes. Non-zero magnetic field breaks the symmetry of the system leading to asymmetric profiles of m_x and m_z. The spikes in m_z are equally spaced in time for $H_0 = 0$ T. On the other hand, for $H_0 > 0$, the two spikes of each oscillation cycle are close to each other but far from those of the previous or next cycle. This is mainly due to the varying effects of the torque due to $\mathbf{H}_a$ as the magnetic octupole traverses the two energy wells.

Finally, in the non-linear regime, higher H_0 leads to lower f, at a fixed J_s, as depicted clearly in the inset of Fig. 12. This is because the barrier height at $\varphi_{\mathrm{oct}} = 360^\circ$ increases with an increase in H_0, thereby requiring higher input energy in order to achieve the same oscillation frequency. As current-driven oscillations are accompanied by large m_z, a strong exchange field along the z-

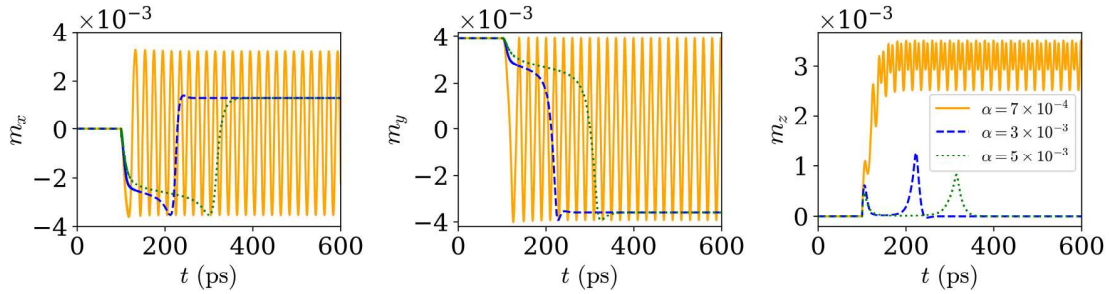

FIG. 15. The three components of the average magnetization, **m**, as a function of time for three different values of the Gilbert damping constant, α. Here, $H_0 = 0.1$ T and $J_s = 2\,\mathrm{MA/cm^2}$ are both applied to the equilibrium state of Fig. 2(c) at $t = 100$ ps. In the case of $\alpha = 0.003$ and 0.005, the magnetic octupole moment switches to the same final steady state in the other energy well. Switching time increases with α. On the other hand, for $\alpha = 0.0007$, chiral oscillations with large m_z are observed.

direction affects the dynamics. However, since such an exchange energy interaction is not included in Eq. (2), and consequently in Eq. (5), our model cannot be used to obtain a unified model of f as a function of H_0 and J_s.

IV. EFFECT OF DAMPING

The results presented in this work, so far, correspond to a Gilbert damping constant of $\alpha = 0.003$, which has previously been used for numerical analysis in Refs. 19, 29 and 36. On the other hand, a lower damping constant of $\alpha = 0.0007$ was used in other recent works.[21,30] In particular in Ref. 30, it was shown through numerical simulations that for $\alpha = 0.0007$, as compared to $\alpha = 0.003$, the lower limit of external magnetic field for deterministic switching was a non-zero value. That is, for low values of $H_0 \gtrsim 0$, the magnetic octupole moment cannot be deterministically switched. Instead, it exhibits either a stationary steady state or chiral oscillation depending on the magnitude of the input current. This behavior is distinct from that presented in Figs. 8 and 10. Therefore, we numerically investigate the dependence of the final steady states and the threshold currents on α.

Figure 15 shows the three components of the average magnetization vector, **m**, for different values of α but the same values of H_0 and J_s. In the case of $\alpha = 5 \times 10^{-3}$, for $J_s = 2\,\mathrm{MA/cm^2}$ and $H_0 = 0.1$ T applied at $t = 100$ ps, the AFM magnetization switches to a steady state in the other energy well. This is signified by a change in the sign of m_y. As shown by the dashed blue curve and dotted green curve, the final steady state for $\alpha = 5 \times 10^{-3}$ is exactly the same as that obtained for $\alpha = 3 \times 10^{-3}$. The switching time, however, is longer in the case of higher damping since t_{sw} is directly proportional to α [Eq. (8)]. On the other hand, for the case of lower damping, namely, $\alpha = 7 \times 10^{-4}$, the magnetic octupole moment exhibits chiral oscillations when $J_s = 2\,\mathrm{MA/cm^2}$ and $H_0 = 0.1$ T are applied at $t = 100$ ps. This suggests that for lower damping, the threshold currents are lower than those predicted by Eq. (7) and could be dependent on α. It can also be observed that for $\alpha = 7 \times 10^{-4}$, the oscillating m_z is rather large. This suggests that the out-of-(Kagome)-plane exchange interaction plays a major role in the oscillation dynamics, similar to that discussed in Sec. III C.

To further elucidate this dependence of the dynamics on α, we present the phase space of the steady states as a function of J_s and H_0 for various α values in Fig. 16. Notably, the phase space analysis reveals an additional dynamical regime, labeled as IV, for

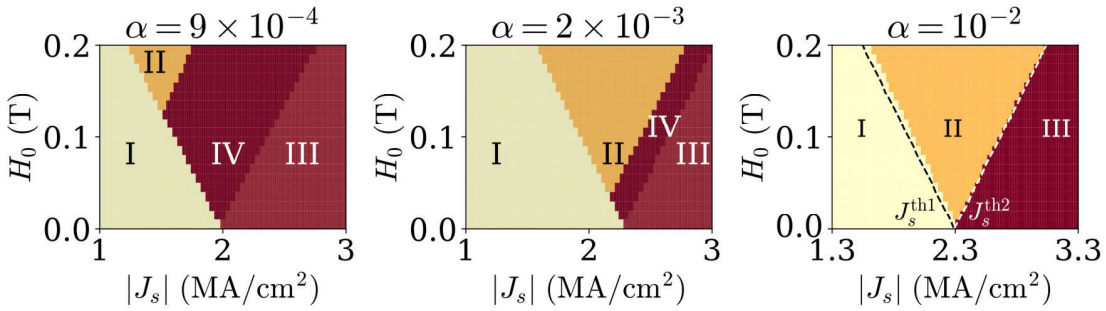

FIG. 16. Final steady state as a function of the input current J_s and applied magnetic fields for different Gilbert damping constant. Here, I and II represent the case of no switching and switching while both III and IV correspond to chiral oscillation. The black dashed lines superimposed on the phase space, in the case of $\alpha = 0.01$, are the two threshold currents, as discussed in the case of $\alpha = 3 \times 10^{-3}$.

$\alpha = 9 \times 10^{-4}$ and 2×10^{-3}, alongside the three previously identified regimes observed for $\alpha = 3 \times 10^{-3}$, and also found in the case of $\alpha = 0.01$. As highlighted earlier for $\alpha = 0.003$, region I represents stationary steady states in the proximity of the initial ground states, for $\varphi_{oct}^{init} = 90°$ ($\varphi_{oct}^{init} = 270°$) and $J_s > 0$ ($J_s < 0$). Region II, on the other hand, corresponds to deterministic switching between the two stable states, while the magnetic octupole moment exhibits chiral oscillations in region III, regardless of the initial state or the direction of J_s, as long as $|J_s|$ exceeds the highest threshold current. Interestingly, in region IV, chiral oscillations occur for $\varphi_{oct}^{init} = 90°$ ($\varphi_{oct}^{init} = 270°$) and $J_s > 0$ ($J_s < 0$), while only stationary states are observed for $\varphi_{oct}^{init} = 270°$ ($\varphi_{oct}^{init} = 90°$). This scenario is vividly depicted in Fig. 17 for $\alpha = 9 \times 10^{-4}$, $|J_s| = 1.72\,\mathrm{MA/cm^2}$ and $H_0 = 0.1\,\mathrm{T}$.

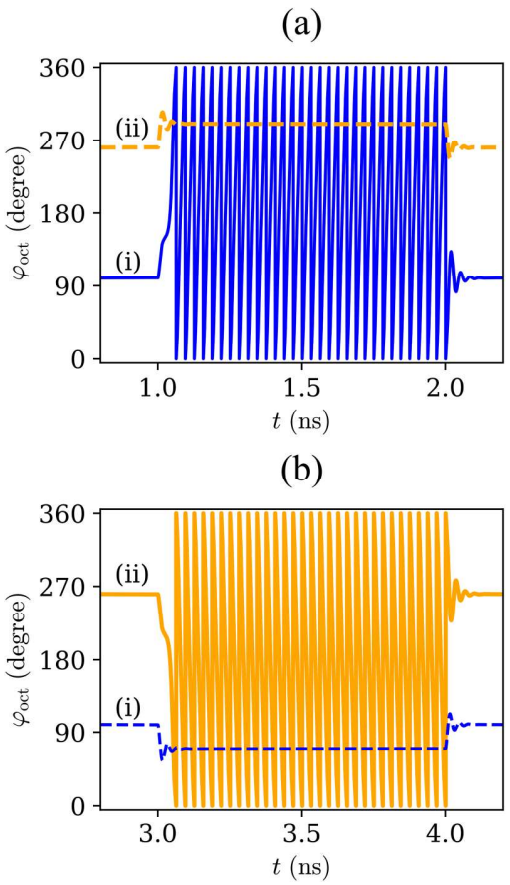

FIG. 17. Steady-state dynamics of the magnetic octupole moment as a function of time for $\alpha = 9 \times 10^{-4}$. (i) and (ii): Possible ground states for $H_0 = 0.1\,\mathrm{T}$ in the negative x-direction. (a) The pulse is turned on at $t = 1\,\mathrm{ns}$ to $J_s = 1.72\,\mathrm{MA/cm^2}$ and turned off at $t = 2\,\mathrm{ns}$. Steady-state oscillations for (i) but not for (ii). (b) The pulse is turned on at $t = 3\,\mathrm{ns}$ to $J_s = -1.72\,\mathrm{MA/cm^2}$ and turned off at $t = 4\,\mathrm{ns}$. Steady-state oscillations for (ii) but not for (i).

In contrast to the scenario with high damping, where the three regimes were distinguished by two threshold currents, the presence of four regimes in the low α case is marked by three distinct threshold currents. Although all the three threshold currents seem to scale linearly with H_0 for $\alpha \lesssim 2 \times 10^{-3}$, it can be clearly observed that they depend on the Gilbert damping constant, unlike Eq. (7). Moreover, for low values of H_0, deterministic switching is not possible; instead the magnetic octupole moment can only exhibit oscillation dynamics above the threshold current. Deterministic switching between the two stable states of PMA Mn_3Sn becomes feasible again for larger values of H_0. This lower limit of H_0 for deterministic switching dynamics decreases as α increases. Although further analytic investigation is required to understand the dependence of the dynamics on the damping constant, we suspect that in region I the net input energy is low; therefore, the magnetic octupole moment cannot overcome the barrier at 180°. On the other hand, in region III the net input energy is very high such that magnetic octupole moment can exhibit sustained oscillations. In region IV, for low H_0, the barrier at 180° is lowered which enables deterministic switching to the other energy well. However, the low damping of the system possibly does not dissipate enough energy of the magnetic octupole moment, and therefore, it goes over the barrier at 360° due to its inertia. This leads to sustained oscillations. For higher fields, the barrier at 360° becomes significantly large and the magnetic octupole cannot overcome it, such that deterministic switching becomes possible. Finally, we found that for $\alpha = 0.01$, the analysis presented in Sec. III holds true. Since this analysis is true for both $\alpha = 3 \times 10^{-3}$ and $\alpha = 10^{-2}$, it is applicable for all other values of damping constants between them.

V. CONCLUSION

Mn_3Sn is a metallic antiferromagnet that shows large AHE, ANE, and MOKE signals. In addition, the octupole states can be detected via TMR in an all-antiferromagnetic tunnel junction comprising two layers of Mn_3Sn with an insulator layer sandwiched between them. Bulk Mn_3Sn has a 120° anti-chiral structure; however, a competition between the local anisotropy and the DMI leads to the existence of a small net magnetization, which is sixfold degenerate. Application of strain to bulk Mn_3Sn reduces its symmetry from sixfold to twofold degenerate and provides a way to control the strength of the net magnetization as well as that of the AHE signal. In this work, we analyzed the case of both uniaxial compressive and tensile strains and discussed the dependence of the magnetic octupole moment on the strain as well as on the external field. Since a recent experiment reported tensile strain in epitaxial Mn_3Sn grown on the (110)[001] MgO substrate, we numerically and analytically explored the field-assisted SOT driven dynamics in monodomain Mn_3Sn with tensile strain. We found that the magnetic octupole moment exhibits either a stationary state or chiral oscillations in the absence of a symmetry-breaking field. On the other hand, when an external field is applied, in addition to the stationary state and chiral oscillations, the magnetic octupole moment can also be deterministically switched between the two stable states for a range of currents. We derived an effective equation, which accurately predicts the stationary states in both

energy wells. We also derived simple analytic expressions of the threshold currents and found them to agree very well against the numerical results for small external magnetic fields. We obtained a functional form of the switching time as a function of the material parameters and the external stimuli and found it to match very well against numerical data. The frequency of chiral oscillations, which can be tuned from 100s of MHz to 10s of GHz range, was found to vary non-linearly closer to the threshold current and linearly for larger input currents. Further, through numerical simulations, we showed that the order dynamics is dependent on the Gilbert damping for lower values of α. For the sake of a complete picture, we also explored the field-assisted switching dynamics in thin films of Mn_3Sn with no strain as well as compressive strain and presented the relevant results in the supplementary material. We expect the insights of our theoretical investigation to be useful to both theorists and experimentalists in their exploration of the interplay of field-assisted SOT and the order dynamics in Mn_3Sn, and further benchmarking the device performance.

SUPPLEMENTARY MATERIAL

See the supplementary material for the perturbative analysis of the ground state, the SOT-driven dynamics of thin films of Mn_3Sn with compressive strain as well as no strain, and a brief discussion of the AHE and TMR detection schemes.

ACKNOWLEDGMENTS

This research was supported by the NSF through the University of Illinois at Urbana-Champaign Materials Research Science and Engineering Center (No. DMR-1720633).

AUTHOR DECLARATIONS

Conflict of Interest

The authors have no conflicts to disclose.

Author Contributions

Ankit Shukla: Conceptualization (equal); Data curation (equal); Formal analysis (equal); Investigation (equal); Methodology (equal); Software (equal); Validation (equal); Visualization (equal); Writing – original draft (equal); Writing – review & editing (equal). **Siyuan Qian:** Data curation (equal); Formal analysis (equal); Investigation (equal); Software (equal); Validation (equal). **Shaloo Rakheja:** Conceptualization (lead); Formal analysis (equal); Funding acquisition (lead); Investigation (equal); Project administration (lead); Supervision (lead); Writing – original draft (equal); Writing – review & editing (equal).

DATA AVAILABILITY

The data that support the findings of this study are available from the corresponding author upon reasonable request.

REFERENCES

[1]E. Gomonay and V. Loktev, "Spintronics of antiferromagnetic systems," Low Temp. Phys. **40**, 17–35 (2014).
[2]T. Jungwirth, X. Marti, P. Wadley, and J. Wunderlich, "Antiferromagnetic spintronics," Nat. Nanotechnol. **11**, 231 (2016).
[3]V. Baltz, A. Manchon, M. Tsoi, T. Moriyama, T. Ono, and Y. Tserkovnyak, "Antiferromagnetic spintronics," Rev. Mod. Phys. **90**, 015005 (2018).
[4]M. B. Jungfleisch, W. Zhang, and A. Hoffmann, "Perspectives of antiferromagnetic spintronics," Phys. Lett. A **382**, 865–871 (2018).
[5]J. Han, R. Cheng, L. Liu, H. Ohno, and S. Fukami, "Coherent antiferromagnetic spintronics," Nat. Mater. **22**, 1–12 (2023).
[6]W. Zhang, W. Han, S.-H. Yang, Y. Sun, Y. Zhang, B. Yan, and S. S. Parkin, "Giant facet-dependent spin-orbit torque and spin Hall conductivity in the triangular antiferromagnet $IrMn_3$," Sci. Adv. **2**, e1600759 (2016).
[7]J. Kübler and C. Felser, "Non-collinear antiferromagnets and the anomalous Hall effect," Europhys. Lett. **108**, 67001 (2014).
[8]Y. Zhang, Y. Sun, H. Yang, J. Železnỳ, S. P. Parkin, C. Felser, and B. Yan, "Strong anisotropic anomalous Hall effect and spin Hall effect in the chiral antiferromagnetic compounds Mn_3X (X = Ge, Sn, Ga, Ir, Rh, and Pt)," Phys. Rev. B **95**, 075128 (2017).
[9]H. Iwaki, M. Kimata, T. Ikebuchi, Y. Kobayashi, K. Oda, Y. Shiota, T. Ono, and T. Moriyama, "Large anomalous Hall effect in L12-ordered antiferromagnetic Mn_3Ir thin films," Appl. Phys. Lett. **116**, 022408 (2020).
[10]H. Tsai, T. Higo, K. Kondou, S. Sakamoto, A. Kobayashi, T. Matsuo, S. Miwa, Y. Otani, and S. Nakatsuji, "Large Hall signal due to electrical switching of an antiferromagnetic Weyl semimetal state," Small Sci. **1**, 2000025 (2021).
[11]T. Higo, H. Man, D. B. Gopman, L. Wu, T. Koretsune, O. M. J. van't Erve, Y. P. Kabanov, D. Rees, Y. Li, M.-T. Suzuki, S. Patankar, M. Ikhlas, C. L. Chien, R. Arita, R. D. Shull, J. Orenstein, and S. Nakatsuji, "Large magneto-optical Kerr effect and imaging of magnetic octupole domains in an antiferromagnetic metal," Nat. Photonics **12**, 73–78 (2018).
[12]J. Železnỳ, Y. Zhang, C. Felser, and B. Yan, "Spin-polarized current in noncollinear antiferromagnets," Phys. Rev. Lett. **119**, 187204 (2017).
[13]X. Wang, M. T. Hossain, T. R. Thapaliya, D. Khadka, S. Lendinez, H. Chen, M. F. Doty, M. B. Jungfleisch, S. X. Huang, X. Fan, and J. Q. Xiao, "Spin currents with unusual spin orientations in noncollinear Weyl antiferromagnetic Mn_3Sn," Phys. Rev. Mater. **7**, 034404 (2023).
[14]P. Qin, H. Yan, X. Wang, H. Chen, Z. Meng, J. Dong, M. Zhu, J. Cai, Z. Feng, X. Zhou, L. Liu, T. Zhang, Z. Zeng, J. Zhang, C. Jiang, and Z. Liu, "Room-temperature magnetoresistance in an all-antiferromagnetic tunnel junction," Nature **613**, 485–489 (2023).
[15]X. Chen, T. Higo, K. Tanaka, T. Nomoto, H. Tsai, H. Idzuchi, M. Shiga, S. Sakamoto, R. Ando, H. Kosaki, T. Matsuo, D. Nishio-Hamane, R. Arita, S. Miwa, and S. Nakatsuji, "Octupole-driven magnetoresistance in an antiferromagnetic tunnel junction," Nature **613**, 490–495 (2023).
[16]Y. Yamane, O. Gomonay, and J. Sinova, "Dynamics of noncollinear antiferromagnetic textures driven by spin current injection," Phys. Rev. B **100**, 054415 (2019).
[17]S. Tomiyoshi and Y. Yamaguchi, "Magnetic structure and weak ferromagnetism of Mn_3Sn studied by polarized neutron diffraction," J. Phys. Soc. Jpn. **51**, 2478–2486 (1982).
[18]N. H. Sung, F. Ronning, J. D. Thompson, and E. D. Bauer, "Magnetic phase dependence of the anomalous Hall effect in Mn_3Sn single crystals," Appl. Phys. Lett. **112**, 132406 (2018).
[19]H. Tsai, T. Higo, K. Kondou, T. Nomoto, A. Sakai, A. Kobayashi, T. Nakano, K. Yakushiji, R. Arita, S. Miwa, Y. Otani, and S. Nakatsuji, "Electrical manipulation of a topological antiferromagnetic state," Nature **580**, 608–613 (2020).
[20]Y. Takeuchi, Y. Yamane, J.-Y. Yoon, R. Itoh, B. Jinnai, S. Kanai, J. Ieda, S. Fukami, and H. Ohno, "Chiral-spin rotation of non-collinear antiferromagnet by spin–orbit torque," Nat. Mater. **20**, 1364–1370 (2021).
[21]B. Pal, B. K. Hazra, B. Göbel, J.-C. Jeon, A. K. Pandeya, A. Chakraborty, O. Busch, A. K. Srivastava, H. Deniz, and J. M. Taylor, "Setting of the magnetic structure of chiral kagome antiferromagnets by a seeded spin-orbit torque," Sci. Adv. **8**, eabo5930 (2022).
[22]G. K. Krishnaswamy, G. Sala, B. Jacot, C.-H. Lambert, R. Schlitz, M. D. Rossell, P. Nöel, and P. Gambardella, "Time-dependent multistate

switching of topological antiferromagnetic order in Mn_3Sn," Phys. Rev. Appl. **18**, 024064 (2022).
[23]T. Xu, H. Bai, Y. Dong, L. Zhao, H.-A. Zhou, J. Zhang, X.-X. Zhang, and W. Jiang, "Robust spin torque switching of noncollinear antiferromagnet Mn_3Sn," APL Mater. **11**, 071116 (2023).
[24]R. Ramaswamy, J. M. Lee, K. Cai, and H. Yang, "Recent advances in spin-orbit torques: Moving towards device applications," Appl. Phys. Rev. **5**, 031107 (2018).
[25]G. Q. Yan, S. Li, H. Lu, M. Huang, Y. Xiao, L. Wernert, J. A. Brock, E. E. Fullerton, H. Chen, H. Wang, and C. R. Du, "Quantum sensing and imaging of spin–orbit-torque-driven spin dynamics in the non-collinear antiferromagnet Mn_3Sn," Adv. Mater. **34**, 2200327 (2022).
[26]A. Markou, J. Taylor, A. Kalache, P. Werner, S. Parkin, and C. Felser, "Noncollinear antiferromagnetic Mn_3Sn films," Phys. Rev. Mater. **2**, 051001 (2018).
[27]J. Liu, Z. Zhang, M. Fu, X. Zhao, R. Xie, Q. Cao, L. Bai, S. Kang, Y. Chen, S. Yan *et al.*, "The anomalous Hall effect controlled by residual epitaxial strain in antiferromagnetic Weyl semimetal Mn_3Sn thin films grown by molecular beam epitaxy," Res. Phys. **52**, 106803 (2023).
[28]M. Ikhlas, S. Dasgupta, F. Theuss, T. Higo, S. Kittaka, B. Ramshaw, O. Tchernyshyov, C. Hicks, and S. Nakatsuji, "Piezomagnetic switching of the anomalous Hall effect in an antiferromagnet at room temperature," Nat. Phys. **18**, 1086–1093 (2022).
[29]S. Dasgupta and O. A. Tretiakov, "Tuning the Hall response of a noncollinear antiferromagnet via spin-transfer torques and oscillating magnetic fields," Phys. Rev. Res. **4**, L042029 (2022).
[30]T. Higo, K. Kondou, T. Nomoto, M. Shiga, S. Sakamoto, X. Chen, D. Nishio-Hamane, R. Arita, Y. Otani, S. Miwa *et al.*, "Perpendicular full switching of chiral antiferromagnetic order by current," Nature **607**, 474–479 (2022).
[31]J.-Y. Yoon, P. Zhang, C.-T. Chou, Y. Takeuchi, T. Uchimura, J. T. Hou, J. Han, S. Kanai, H. Ohno, S. Fukami, and L. Liu, "Handedness anomaly in a non-collinear antiferromagnet under spin–orbit torque," Nat. Mater. **22**, 1106–1113 (2023).
[32]J. Dong, X. Li, G. Gurung, M. Zhu, P. Zhang, F. Zheng, E. Y. Tsymbal, and J. Zhang, "Tunneling magnetoresistance in noncollinear antiferromagnetic tunnel junctions," Phys. Rev. Lett. **128**, 197201 (2022).
[33]H. V. Gomonay, R. V. Kunitsyn, and V. M. Loktev, "Symmetry and the macroscopic dynamics of antiferromagnetic materials in the presence of spin-polarized current," Phys. Rev. B **85**, 134446 (2012).
[34]O. Gomonay and V. Loktev, "Using generalized landau-lifshitz equations to describe the dynamics of multi-sublattice antiferromagnets induced by spin-polarized current," Low Temp. Phys. **41**, 698–704 (2015).
[35]A. Shukla and S. Rakheja, "Spin-torque-driven terahertz auto-oscillations in noncollinear coplanar antiferromagnets," Phys. Rev. Appl. **17**, 034037 (2022).
[36]A. Shukla, S. Qian, and S. Rakheja, "Order parameter dynamics in Mn_3Sn driven by DC and pulsed spin–orbit torques," APL Mater. **11**, 091110 (2023).
[37]Z. Xu, X. Zhang, Y. Qiao, G. Liang, S. Shi, and Z. Zhu, "Deterministic spin-orbit torque switching of Mn_3Sn with the interplay between spin polarization and kagome plane," arXiv:2308.08091 (2023).
[38]J. Liu and L. Balents, "Anomalous Hall effect and topological defects in antiferromagnetic Weyl semimetals: Mn_3Sn/Ge," Phys. Rev. Lett. **119**, 087202 (2017).
[39]X. Li, S. Jiang, Q. Meng, H. Zuo, Z. Zhu, L. Balents, and K. Behnia, "Free energy of twisting spins in Mn_3Sn," Phys. Rev. B **106**, L020402 (2022).
[40]P. Zhang, "Current-induced dynamics of easy-plane antiferromagnets," Ph.D. thesis (Massachusetts Institute of Technology, 2023).
[41]M.-T. Suzuki, T. Koretsune, M. Ochi, and R. Arita, "Cluster multipole theory for anomalous Hall effect in antiferromagnets," Phys. Rev. B **95**, 094406 (2017).
[42]I. D. Mayergoyz, G. Bertotti, and C. Serpico, *Nonlinear Magnetization Dynamics in Nanosystems* (Elsevier, 2009).
[43]K.-S. Lee, S.-W. Lee, B.-C. Min, and K.-J. Lee, "Threshold current for switching of a perpendicular magnetic layer induced by spin Hall effect," Appl. Phys. Lett. **102**, 112410 (2013).